



Polar nematic phase in short-chained fluorinated hydrogen-bonded liquid crystals

Malek Fouzai, Philippe Dieudonné-George, Ahlem Guesmi, Naoufel Ben Hamadi, Youssef Arfaoui, Taoufik Soltani, Yves Chevalier

► To cite this version:

Malek Fouzai, Philippe Dieudonné-George, Ahlem Guesmi, Naoufel Ben Hamadi, Youssef Arfaoui, et al.. Polar nematic phase in short-chained fluorinated hydrogen-bonded liquid crystals. *Journal of Molecular Liquids*, 2023, 375, pp.121307. 10.1016/j.molliq.2023.121307 . hal-03978339

HAL Id: hal-03978339

<https://hal.science/hal-03978339>

Submitted on 8 Feb 2023

HAL is a multi-disciplinary open access archive for the deposit and dissemination of scientific research documents, whether they are published or not. The documents may come from teaching and research institutions in France or abroad, or from public or private research centers.

L'archive ouverte pluridisciplinaire **HAL**, est destinée au dépôt et à la diffusion de documents scientifiques de niveau recherche, publiés ou non, émanant des établissements d'enseignement et de recherche français ou étrangers, des laboratoires publics ou privés.

Polar Nematic Phase in Short-Chained Fluorinated Hydrogen-Bonded Liquid Crystals

Malek Fouzai¹, Philippe Dieudonné-George², Ahlem Guesmi³, Naoufel Ben Hamadi³, Youssef Arfaoui⁴, Taoufik Soltani^{1,*}, Yves Chevalier⁵

¹ Université de Tunis El Manar, Faculté des Sciences de Tunis, Laboratoire de Physique de la Matière Molle et de la Modélisation Électromagnétique (LR99ES16), 2092 Tunis, Tunisia.

² Laboratoire Charles Coulomb, UMR 5221, CNRS-Université de Montpellier, 34095 Montpellier, France.

³ Chemistry Department, College of Science, Imam Mohammad Ibn Saud Islamic University (IMSIU), Riyadh, Kingdom of Saudi Arabia.

⁴ Université de Tunis El Manar, Faculté des Sciences de Tunis, Laboratoire de Caractérisations, Applications et Modélisation de Matériaux (LR18ES08), 2092 Tunis, Tunisia.

⁵ Université Claude Bernard Lyon 1, Laboratoire d'Automatique, de Génie des Procédés et de Génie Pharmaceutique (LAGEPP), CNRS UMR 5007, 43 bd 11 Novembre, 69622 Villeurbanne Cedex, France.

Correspondence: taoufik.soltani@fst.utm.tn

Abstract: So as to investigate structure-activity relationships in hydrogen bonded liquid crystals, a new short-chained (7 carbon atoms) fluorinated hydrogen-bonded liquid crystal 4-heptyloxy-2-fluorobenzoic acid, 7OBAF, is prepared. Differential scanning calorimetry, polarized optical microscopy and X-ray diffraction disclose a phase sequence as two crystalline, a nematic and the isotropic phases. Dielectric spectroscopy of the nematic phase in the frequency range of 1 Hz–6 MHz reveals a low frequency mode ascribed to ferroelectric clusters. A high polarization is induced by an external electric field, in agreement with results of dielectric measurements. Such polarization increases as the alkyl chain length is shorter. Results of DFT calculations using the Maier–Meier relationship are consistent with the dielectric measurements; they reveal the parallel molecular distribution and provide the dipole moment, polarization anisotropy, birefringence and dielectric anisotropy. Intermolecular hydrogen bonds linking the fluorine substituent and the aromatic hydrogen atoms are also disclosed.

Keywords: Nematic liquid crystal; dielectric; polarization; DFT

1. Introduction

The nematic liquid crystalline (LC) phase is characterized by high fluidity and orientational ordering leading to anisotropic behavior, which confers interesting optical, dielectric, and viscoelastic properties. In the nematic phase, molecules of liquid crystal are oriented on average along a common direction, called the director, and their alignment is easily distorted by external electric or magnetic fields due to the weak orientational elasticity. A linear and rigid part of molecule made of several conjugated multiple bonds and aromatic rings ensures the thermal stability of this phase [1–19]. Polar, rod-like LC materials have attracted considerable attention as a promising candidate material for next generations of displays as they exhibit new types of nematic phases. Therefore, many works have been devoted in past years on new LC materials forming a nematic phase in order to extend the range of available properties and open new applications.

Variants of the classical nematic phase having unusual properties have recently been disclosed for polar molecules. Mandle et al. have shown the existence of two different nematic mesophases (denoted N and N_x) separated by a weakly first-order transition for a polar rod-like liquid crystalline LC material [20,21]. Moreover, a ferroelectric-like polar arrangement of fluorinated calamatic liquid crystals have been reported by Nishikawa et al. [22]. They considered that these materials possess many finely divided ferroelectric domains that grow and agglomerate under an electric field. More recently, the polar ordering in nematic phases has been observed by our group [17,23]. The stabilization of this type of nematic phase, called cybotactic, is most often attributed to the presence of ferroelectric clusters. Recently, a new type of ferroelectric nematic phase (N_f) has been theoretically predicted and experimentally confirmed by Chen et al. [24]. They found that this phase obtained by cooling the natural nematic phase had a spontaneous reorientable polarization parallel to the director. Theoretical simulations revealed that short-range polar molecular interactions were the origin of the appearance of this ferroelectric nematic phase. Manabe et al. have demonstrated that the strong dipole moment plays a definite role in the stabilization of this new phase [25]. In addition, Mandle et al. reported a nematic-nematic transition between the usual nematic (N_u) at higher temperature and a splay nematic (N_s) with high dielectric constant at lower temperature [26]. Finally, fluorinated LCs have been reported by Saha et al. to show multiple nematic phases with three distinct ferroelectric states, F₁, F₂ and F₃ [27].

Although a ferroelectric nematic phase in which all dipoles point in the same direction has been theoretically predicted by Born in 1916 based on the interaction of molecular electric dipoles

[28], such a phase has only been experimentally observed recently. Another phenomenon of electro-convection (EC) has also been observed and extensively studied [29–34]. Therefore, a variety of pattern morphologies has been disclosed by polarized optical microscopy, and the frequency and amplitude of the electric field-induced patterns have been discussed. Generally, this phenomenon has been observed in LCs doped by dyes, electrolytes, nanoparticles, and nanotubes. All these additives contribute to and increase the convection effect [30–33]. Recently, Lee et al. [34] have experimentally observed EC in the pure nematic phase without free charges and proposed a theoretical rationale. Moreover, several theoretical models for the mechanism of EC in liquid crystals have been proposed [30,34,35].

The present research is an extension of the studies of H-bonded liquid crystals using fluorinated alkoxybenzoic acids with alkyl chains of various lengths [23]. Ferroelectric clusters were revealed in these nematic phases, called cybotactic, by a dielectric relaxation in the kHz range. They have been observed for monofluorinated alkoxybenzoic acids having alkyl chain lengths between 8 and 12 carbon atoms, and it has not been observed with non-fluorinated alkoxybenzoic acids. The characteristic dielectric relaxation phenomenon was higher for the compound with the shorter chain length (8 carbons), so that the present work addresses a study of a similar fluorinated compound having a shorter alkyl chain of 7 carbon atoms, namely 4-heptyloxy-2-fluorobenzoic acid (7OBAF), with the expectation of enhancing again the ferroelectric behavior.

The synthesized 7OBAF was characterized by infrared, ^1H , ^{19}F and ^{13}C NMR spectroscopy. The chemical formulae of this compound and its hydrogen-bonded complex are shown in Figure 1. The optical and dielectric properties of the nematic phase were studied experimentally and theoretically using the Maier-Meier equation and Vuks models. Density functional theory (DFT) calculations were used to determine these essential parameters, so as to contribute to a better understanding of the relationships between the molecular structure and the physical properties.

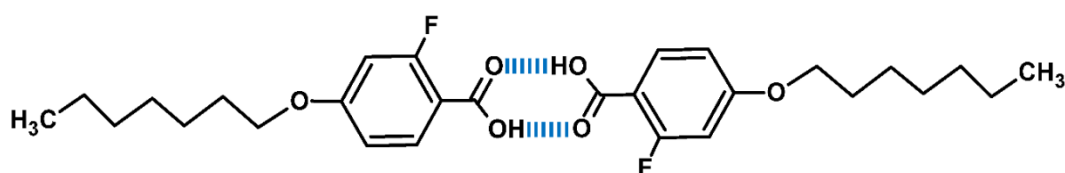


Figure 1. The chemical structure of the hydrogen-bonded complex of 7OBAF.

2. Materials and Methods

2.1. Materials and chemical characterizations

2-fluoro-4-heptyloxybenzoic acid (7OBAF) was synthesized by adding dropwise 1-bromoheptane (15 g, 0.084 mol) to a stirred solution of potassium hydroxide (5.8 g, 0.1 mol), water (10 mL), ethanol (100 mL) and 2-fluoro-4-hydroxybenzoic acid (10 g, 0.064 mol). The solution was heated under reflux for 3 h. After cooling to room temperature, KOH (4 g, 0.07 mol) in 10 mL of water was added and the mixture was again stirred under reflux for 2 h. Then, KOH (5 g) in 5 mL of water was added to the cooled solution and the mixture was heated under reflux for further 2 h. The solvent was evaporated and the mixture was poured onto crushed ice and 35 % HCl. The solid product was filtered off and recrystallized from absolute ethanol.

The resulting compound was characterized by elemental analyses, ^1H , ^{19}F and ^{13}C NMR, and IR spectroscopies in order to confirm its chemical structure.

Carbon and hydrogen elemental analyses (FlashSmartTMCHNS/O elemental analyzer from Thermo Fisher) were performed on two replicates, giving a mean value C: 65.8 %, H: 7.6%, in correct agreement with the theoretical values (C: 66.12 %, H: 7.53 %) calculated from the chemical formula $\text{C}_{14}\text{H}_{19}\text{O}_3\text{F}$.

^1H , ^{19}F and ^{13}C NMR spectra of 7OBAF solution in CDCl_3 were run on a Bruker AVL300 spectrometer working at 300 MHz Larmor frequency for ^1H NMR. Chemical shifts of ^1H and ^{13}C NMR spectra are given in ppm from TMS and those of ^{19}F NMR spectra are given in ppm from CFCl_3 . Their spectra and line assignments are given in [Figure S1 \(SI file\)](#). The non-decoupled ^{19}F NMR spectrum displayed a single line that confirmed that 7OBAF was fluoro-monosubstituted. The ^{19}F line was a double doublet because of the scalar couplings with the vicinal H3 proton ($^3J_{\text{F-H3}} = 12.8$ Hz) and the ortho H6 proton located at 4 bonds from the fluorine atom ($^4J_{\text{F-H6}} = 8.7$ Hz). The chemical shift, multiplicity and line integrals of the ^1H NMR spectrum was in accordance with expectations; the values of the $^3J_{\text{F-H3}}$ and $^4J_{\text{F-H6}}$ were the same as observed in the ^{19}F spectrum. The ^{13}C NMR spectrum (broadband ^1H -decoupled) displayed all the expected lines and couplings of the aromatic ^{13}C nuclei with the ^{19}F nucleus that split the lines into doublets ($^1J_{\text{C2-F}} = 260.32$ Hz, $^2J_{\text{C3-F}} = 25.45$ Hz, $^2J_{\text{C1-F}} = 9.08$ Hz, $^3J_{\text{C4-F}} = 11.62$ Hz, $^3J_{\text{CO2H-F}} = 3.58$ Hz, $^4J_{\text{C5-F}} = 2.77$ Hz, $^4J_{\text{C6-F}} = 2.12$ Hz).

Chemical shifts:

- ^1H NMR (300 MHz, CDCl_3), δ (ppm from TMS): 0.827 (t, 3H, $^3J_{\text{H-H}} = 7.89$ Hz), 1.243 (8H), 1.731 (m, 2H, $^3J_{\text{H-H}} = 6.5$ Hz, $^3J_{\text{H-H}} = 7.4$ Hz), 3.932 (t, 2H, $^3J_{\text{H-H}} = 6.5$ Hz), 6.572 (dd, 1H, $^3J_{\text{H-F}} = 12.8$ Hz, $^4J_{\text{H-H}} = 2.3$ Hz), 6.661 (dd, 1H, $^3J_{\text{H-H}} = 8.9$ Hz, $^4J_{\text{H-H}} = 2.3$ Hz), 7.893 (t, 1H, $^3J_{\text{H-H}} = 8.7$ Hz, $^4J_{\text{H-F}} = 8.7$ Hz).

- ^{13}C NMR (75 MHz, CDCl_3), δ (ppm from TMS): 14.04, 22.58, 31.73, 28.93, 25.86, 28.98, 68.82, 102.78 (d, $^2J_{\text{C-F}} = 25.45$ Hz), 109.53 (d, $^2J_{\text{C-F}} = 9.08$ Hz), 110.75 (d, $^4J_{\text{C-F}} = 2.77$ Hz), 134.04 (d, $^4J_{\text{C-F}} = 2.12$ Hz), 164.29 (d, $^1J_{\text{C-F}} = 260.32$ Hz), 165.11 (d, $^3J_{\text{C-F}} = 11.62$ Hz), 169.80 (d, $^3J_{\text{C-F}} = 3.58$ Hz).
- ^{19}F NMR (282 MHz, CDCl_3), δ (ppm from CFCl_3): -104.937 (dd, $^3J_{\text{F-H}} = 12.8$ Hz, $^4J_{\text{F-H}} = 8.7$ Hz).

The IR spectrum of 7OBAF was recorded in Attenuated Total Reflectance mode (FTIR-ATR) using a Nicolet™ iS50 FT-IR spectrometer. The spectrum displayed in absorption mode was recorded using 64 scans in the range 400–4000 cm^{-1} at a resolution of 2 cm^{-1} . It showed the expected characteristic absorption bands (Figure S2 in SI file): a broad band between 3100 and 3600 cm^{-1} corresponding to the O–H vibrations of the hydrogen-bonded CO_2H , sharp bands at 2920 and 2850 cm^{-1} corresponding to the C–H stretching vibrations. The strong band at 1610 cm^{-1} corresponds to the C=O vibrations of the carboxylic acid involved in a bimolecular cyclic hydrogen bonding complex [18,23].

2.2. Methods

2.2.1 Liquid crystal cells

For optical microscopy and dielectric measurements, 7OBAF was introduced by capillarity at the temperature of the LC isotropic phase glass cells coated with ITO electrodes treated for planar alignment (brushed polymers) and spaced by either 8 μm or 3 μm . The liquid crystal wets the internal surfaces of the measurement cells. Total wetting conditions were also checked by casting a thin film of 7OBAF on ITO and imaging the surface by scanning electron microscopy (Jeol Neoscope JCM5000 working under a 10 kV acceleration). The image of the surface at room temperature revealed a continuous film of platelet-shaped crystals with no cracks or holes (Figure S3 in SI file). The film of the nematic phase at higher temperature probably also totally wets the ITO surface.

2.2.2 Determination of the phase diagram

The liquid crystalline phase transitions of the compound were determined by combining polarizing optical microscopy (POM), differential scanning calorimetry (DSC) and X-ray scattering.

The thermal behavior of filled cells was first investigated either with an Olympus BX51 microscope equipped with a digital CCD camera (Sony) or a LABORLUX 12 POL S microscope (Leitz, Wetzlar, Germany) equipped with a color camera (D90 from Nikon

Corporation, Tokyo, Japan. The temperature of the cells was regulated at 0.1 °C thanks to a HS400 heating and cooling stage with its STC200D controller (Instec, Boulder, CO, USA). Phase transitions were determined by slowly cooling or heating the samples at $\pm 0.1\text{ }^{\circ}\text{C}\cdot\text{min}^{-1}$. The presence of birefringent phases and their alignment along the easy axis of the cell were observed between crossed polarizers.

The phase transitions were further investigated with DSC using a Q2000 DSC system (TA instruments, New Castle, DE, USA). An 11 mg sample was sealed in an aluminum pan. Heating-cooling cycles were carried out at constant temperature rates between 1 to 10 $^{\circ}\text{C}\cdot\text{min}^{-1}$ under nitrogen atmosphere with a 10 min isotherm between heating and cooling. Thermal data were extracted from the second cooling trace. The enthalpy values $\Delta H\text{ (J}\cdot\text{g}^{-1})$ were obtained by the integration of the peak of the transition using TA Universal Analysis 2000 software.

The nature of the (liquid) crystalline phases was confirmed with X-ray scattering in a wide-angle configuration (WAXS). Lindeman glass capillaries (diameter 1.5 mm) were filled by crystalline powder, sealed by flame and placed in an oven regulated at 0.1 °C. A high brightness low power X-ray tube coupled with aspheric multilayer optics (GeniX3D from Xenocs SA, Grenoble, France) delivered an ultralow divergent beam (0.5 mrad, $\lambda = 0.15418\text{ nm}$) of 0.6 mm beam diameter with a flux of 35 Mphotons/s on the sample. Scattered intensity was measured by a 2D “Pilatus” 490×600 pixels detector (Dectris, Baden-Daettwil, Switzerland, pixel size of $172\times 172\text{ }\mu\text{m}^2$) at a typical distance of $\approx 0.2\text{ m}$ from the sample.

2.2.3 Dielectric properties

Synchronous detection (7280 DSP Lock-in amplifier) was used to measure the dielectric properties of the compounds in a frequency range from 1 Hz to 6 MHz. The temperature of the samples was regulated with a controlled hot stage during the dielectric measurements as a function of the temperature. The stability of the temperature was better than $\pm 0.1\text{ }^{\circ}\text{C}$. The polarization reversal current using standard square wave electrical field was measured using a 2 k Ω resistance associated in series with the liquid crystal cell. An Agilent Technologies DSO5052A oscilloscope was used for recording the current response. An arbitrary square wave tension (10 V and 1 Hz) was applied to the cells using a function generator in order to study the response time. A polychromatic light beam centered at 546 nm was used as an input signal. A photodetector (DET36A Si Biased Detector) assembled to a digital storage oscilloscope (Agilent Technologies DSO5052A) was used to detect the output signal. For a maximum transmittance, the studied cells were placed between crossed polarizers and were then set at an

angle of 45 °. The analysis of the output waveform allowed the calculation of the response time. The methods described in [16] were used for the determination of the refractive indices (n_0 and n_e) and the birefringence (Δn).

3. Results

3.1. Thermal behavior

DSC revealed that 7OBAF underwent three phase transitions above room temperature (Figure 2). The higher-temperature transition peaks upon heating (endothermic) and cooling (exothermic) occurred at similar temperatures (≈ 113 °C for N–I and ≈ 90 °C for Cr2–I). On the other hand, even at the slowest cooling rate (1 °C·min⁻¹), the phase transition Cr1–Cr2 at the lowest temperature showed a large hysteresis with an endothermic peak at 76 °C upon heating and an exothermic one at 53 °C upon cooling.

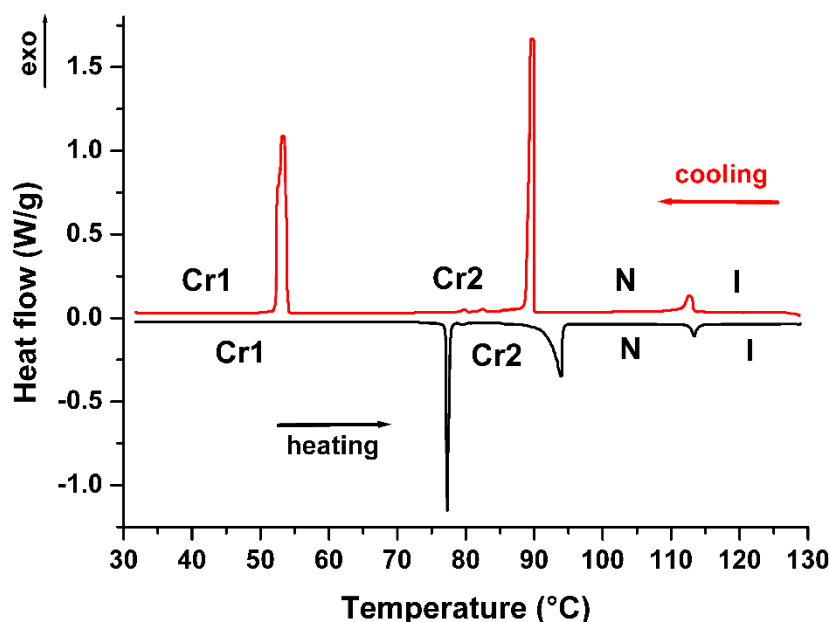


Figure 2. Second heating-cooling DSC trace of 7OBAF at a rate of 1 °C·min⁻¹. The phases are indicated as I (Isotropic), N (Nematic), Cr2 and Cr1 (Crystalline phases).

The hysteresis was confirmed by POM (Figure 3) at the slow cooling rate of 0.1 °C·min⁻¹. Colors due to the birefringence of the crystals indeed strongly changed (Figure 3a,b) at 76 °C when heating the low temperature crystal (Cr1) and at 50 °C when cooling the sample from the high temperature crystal (Cr2) (Figure S4 in SI file). At higher temperatures, the isotropic (I) and nematic (N) phases were easily identified by optical observations between crossed

polarizers. Birefringent needles formed at 93 °C when cooling the nematic phase, which supported the crystalline nature of the intermediate phase (Cr2).

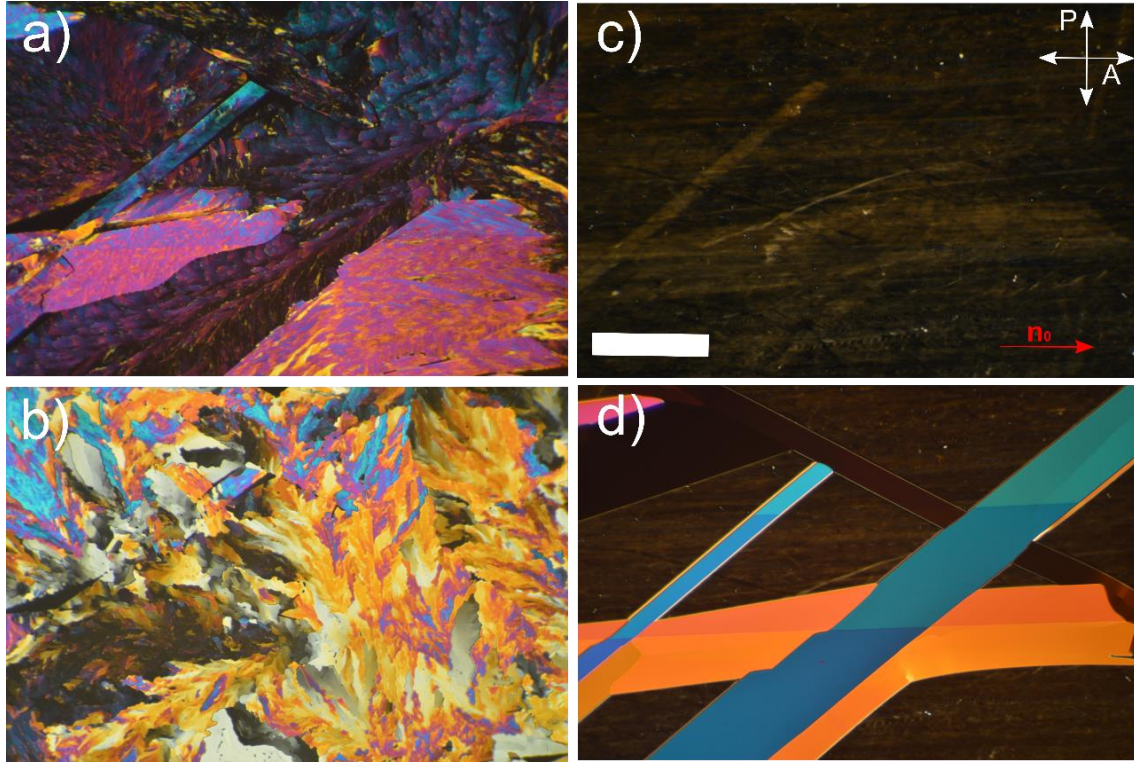


Figure 3. Polarized optical microscopy textures of the same 7OBAF region observed in a 3 μm thick planar cell. Upon heating the phases shown are a) the low-temperature crystalline phase Cr1 at 75 °C, b) the high temperature crystalline phase Cr2 at 80 °C and c) the nematic phase N at 105 °C, which spontaneously aligns along the cell rubbing direction n_0 . d) Under cooling, Cr2 phase appears as needle shape crystals in the background nematic phase at 93 °C. Scale bar = 200 μm .

The presence of two distinct crystalline phases was confirmed by WAXS. [Figure 4](#) shows the evolution of the scattered intensity with increasing temperature. The powder diffraction of crystalline phase Cr1 at 75 °C is quite different from the one of Cr2 at 80 °C.

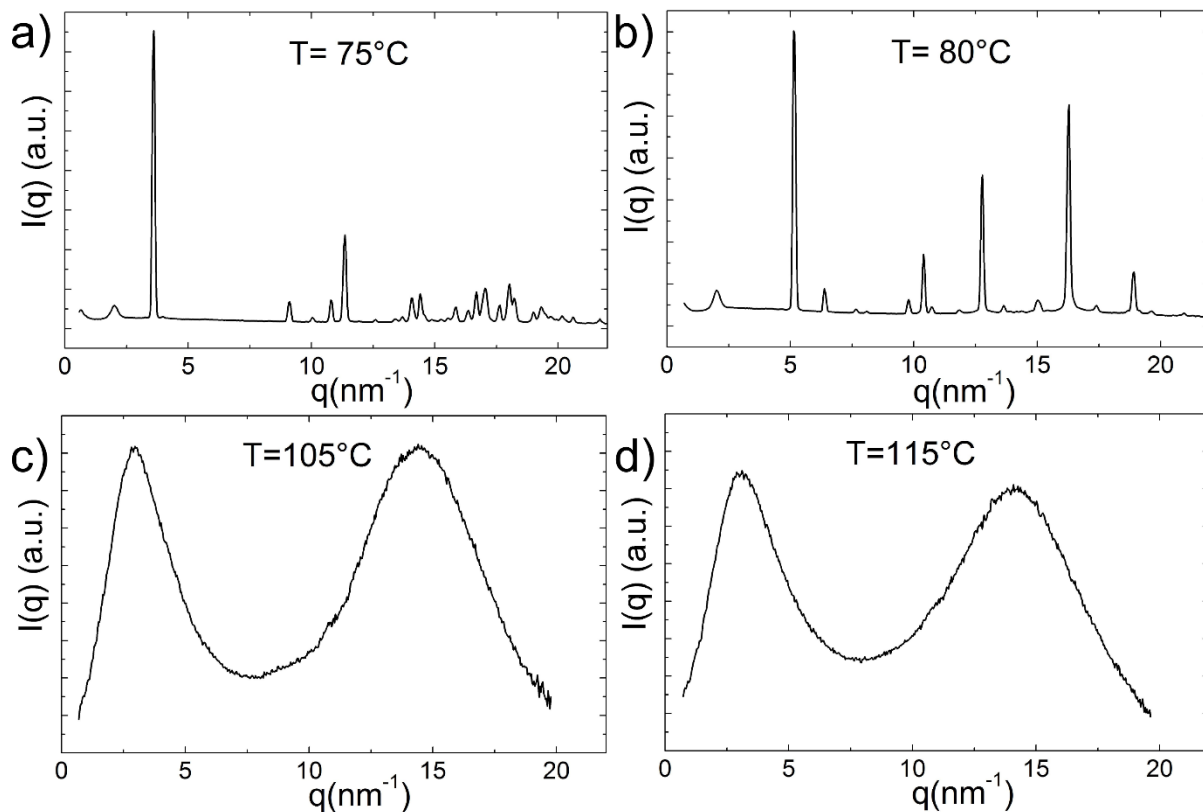


Figure 4. X-ray diffraction powder patterns of the different phases of 7OBAF at increasing temperatures: a) Cr1 (75 °C), b) Cr2 (80 °C), c) N (105 °C), d) I (115 °C). The corresponding 2D patterns are given in [Figure S5 \(SI file\)](#).

From these observations the phase sequence of 7OBAF is given in [Table 1](#), together with the phase sequence of the non-fluorinated homologue 7OBA taken from a previous work [\[14\]](#).

Table 1. Transition temperatures and enthalpies for 7OBAF and 7OBA.

7OBAF						
Transition temperature on heating (°C)	76		94		115	
	Cr1	\rightleftharpoons	Cr2	\rightleftharpoons	N	\rightleftharpoons I
Transition temperature on cooling (°C)	53		90		115	
Enthalpy on cooling (J·g ⁻¹)	57.3		45.6		7.0	
7OBA						
Transition temperature on heating (°C)	91		97		117	
	Cr1	\rightleftharpoons	SmC	\rightleftharpoons	N	\rightleftharpoons I

Compared to 7OBA, the presence of the fluorine atom in 7OBAF not only widened the temperature range of the nematic phase, but also prevented the formation of the SmC phase.

3.2. Dielectric properties

Dielectric spectroscopy was used to study the dielectric relaxation modes over a wide frequency range (1 Hz–6 MHz). Figure 5 shows the frequency dependence of the imaginary permittivity at several temperatures. In the low frequency region ($f \leq 100$ Hz), the measured permittivity was strongly affected by an ionic contribution that decreased with respect to frequency. The dielectric measurements in the nematic phase of 7OBAF revealed two clear molecular relaxation processes. The first one at high frequency (5 MHz) was attributed to the rotation of the molecules around their long molecular axis (soft mode). This relaxation has also been observed in the conventional nematic phase. The second one was observed at low frequencies of about 1 kHz. Such relaxation in the kHz range has already been observed at slightly higher frequency (of the order 10 kHz) for the higher homologues 8OBAF [16] and 10OBAF [23]. It was ascribed to the presence of ferroelectric clusters of a cybotactic nematic phase. Similar behavior has been observed by Mandle et al. [26]. They revealed that the low frequency relaxation mode (800 Hz) appeared as the ferroelectric phase transition was approached upon cooling from the N_u phase. They attributed this behavior to the polar order and splay deformation caused by a flexoelectric phenomenon. It is worth noticing that this mode is a typical property of polar domains specifically detected in ferroelectric [36,37] and ferrielectric [38,39] phases, but not in the paraelectric and conventional nematic phases. In addition, ϵ'' slightly increased with respect to the temperature. The strong value of ϵ'' ($100 < \epsilon'' < 1000$) was similar to the normal nematic phases of the RM734 compound close to the $N-N_s$ transition [26] and the RM734-CN compound [41].

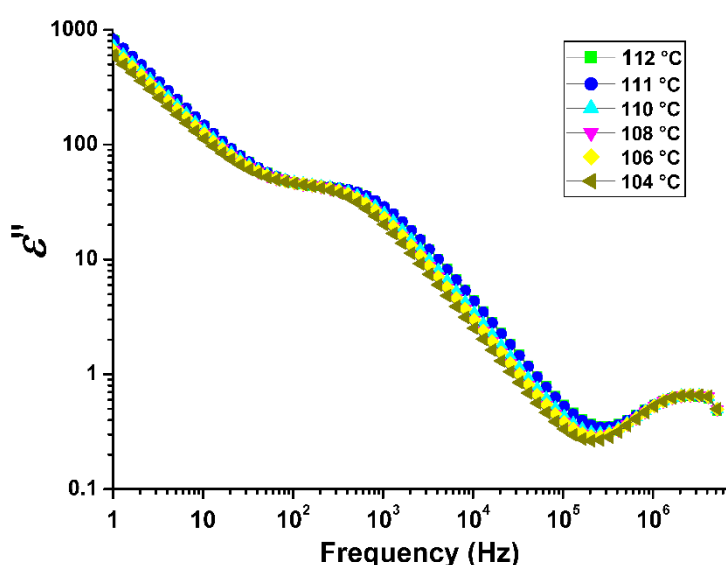


Figure 5. Imaginary permittivity as a function of frequency at six temperatures.

The dielectric anisotropy increased against decreasing temperature (Figure 6). It reached 1.4 at the lowest temperature in the nematic phase. The values were much lower than those observed in 5CB ($\Delta\epsilon=12$) [42].

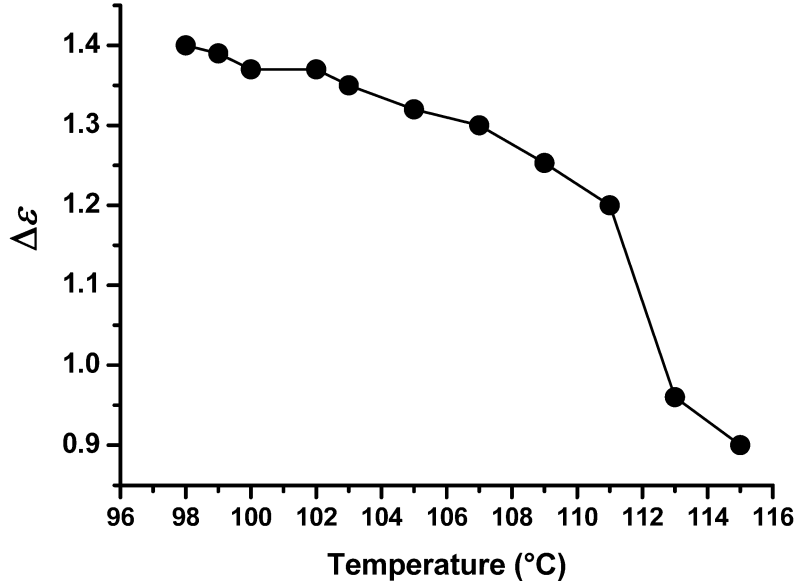


Figure 6. Temperature dependence of dielectric anisotropy for 7OBAF.

3.3. Electro-optic properties

In the absence of an electric field, the macroscopic polarization averaged to zero and the material was macroscopically uniaxial. However, a polarization appeared upon the application of an external field above $1 \text{ V}\cdot\mu\text{m}^{-1}$. POM images did not show stripes separated by lines of defects as Chen et al. [24] have observed. Such stripes were interpreted as domains with alternating directions of ferroelectric polarization. In the present study, application of an electrical field switched the polarization direction in a similar way as the switching of twist bend nematic phases. The temperature dependence of the electrical field $E_s = V_s \cdot d^{-1}$ at the onset of polarization is given in Figure 7. The threshold field decreased slowly from $1.3 \text{ V}\cdot\mu\text{m}^{-1}$ at the highest temperature to $1.1 \text{ V}\cdot\mu\text{m}^{-1}$ at the lowest temperature.

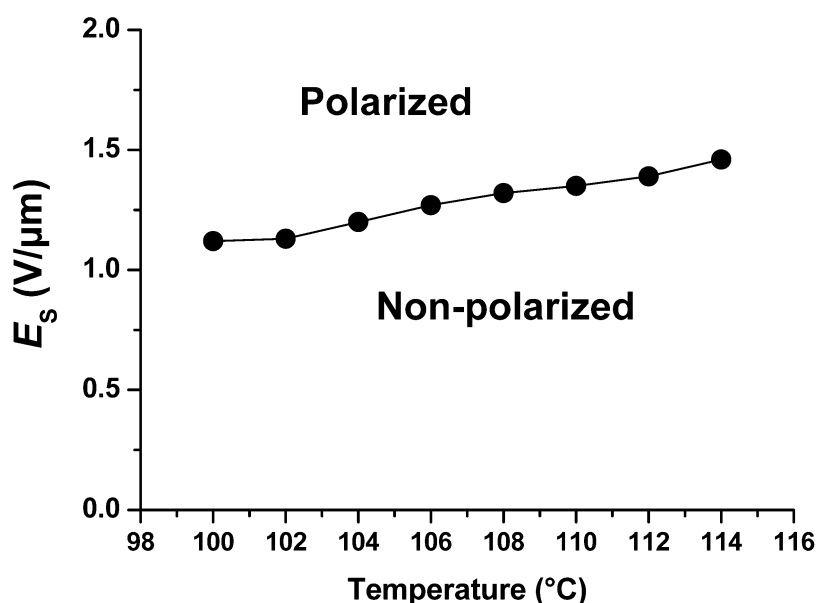


Figure 7. Behavior of the 7OBAF nematic phase in the temperature – electric field space.

The polarization was directly measured from the field-induced current under application of square-wave driving fields in planar alignment, which are commonly used for the polarization measurement process in ferroelectric liquid crystals. Under a square wave field $E = 2 \text{ V} \cdot \mu\text{m}^{-1}$ at 50 Hz, a typical polarization peak was observed (Figure 8). The area of this peak grew upon increasing the voltage until saturation was reached. This behavior was in good agreement with those reported by Chen et al. [24] and Saha et al. [27]. The same measurements with the non-fluorinated homologue compound 8OBA did not show this behavior (Figure 8), indicating that the fluorine atom played an important role in the appearance of polarization. The presence of a polar substituent looked mandatory for such a polarization to occur, in agreement with previous similar observations showing that nitro-, fluoro- or alkyl substitutions were required for polarization to occur [43].

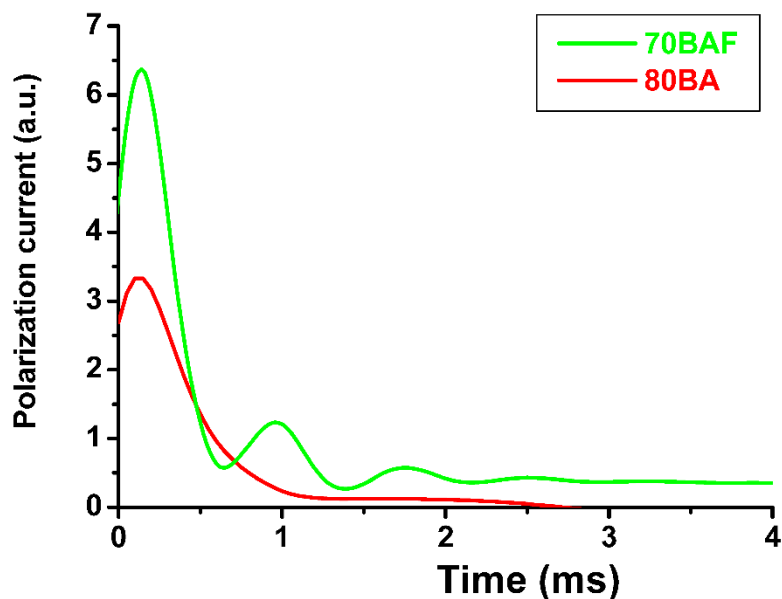


Figure 8. Switching current response of the compounds 7OBAF and 8OBA at 104 °C under a square wave field of $2 \text{ V} \cdot \mu\text{m}^{-1}$.

The polarization (P) at a fixed $E = 2 \text{ V} \cdot \mu\text{m}^{-1}$ continuously decreased as a function of the temperature from a value $P = 2.2 \mu\text{C} \cdot \text{cm}^{-2}$ at low temperature to vanishing values near the N–I phase transition (Figure 9). In addition, the polarization value was higher than that measured with 8OBAF. Polarization was not observed for nOBAF homologues with longer alkyl chain $n \geq 10$. The polarization enhancement with decreasing the chain length is a striking feature of the present study.

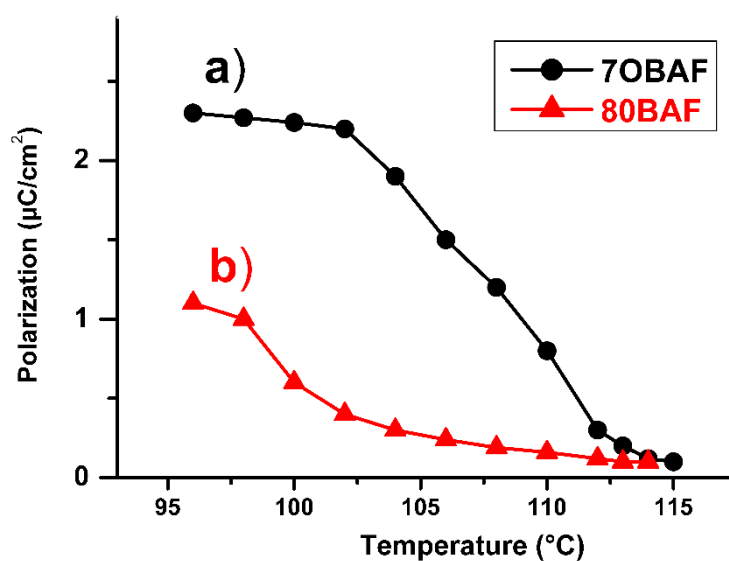


Figure 9. Temperature dependence of the polarization in the nematic phase of a) 7OBAF and b) 8OBAF.

The birefringence of 7OBAF slightly decreased as a function of the temperature from 0.196 at 95 °C down to 0.165 at 116 °C in the isotropic phase (Figure 10a). The values of Δn are comparable to that obtained by Saha et al. [27].

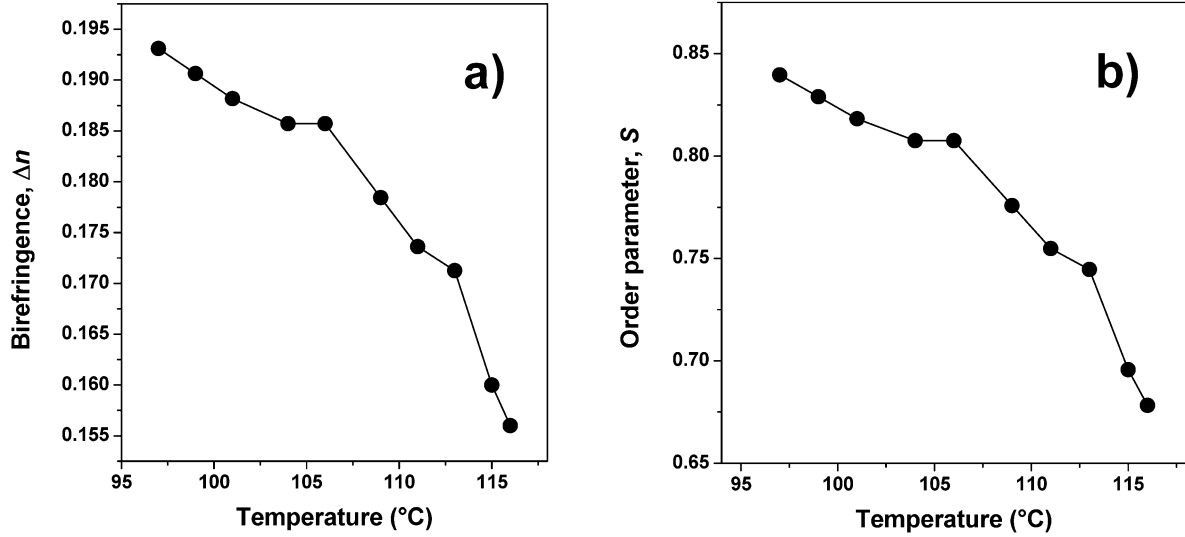


Figure 10. Evolution of a) birefringence Δn and b) order parameter S as a function of temperature.

The order parameter S was calculated from the birefringence values (Figure 10b). The magnitude of S depends on both orientational and conformational averaging, and is proportional to Δn . The temperature dependence of Δn is given by [44,45]:

$$\Delta n = \Delta n_0 (T_C - T)^\beta \quad (1)$$

where β is an exponent characteristic of the material, Δn_0 is the birefringence at 0 K, and T_C is the N–I transition temperature. The best fit of Equation 1 to experimental data in Figure 10a was obtained for $\beta = 0.14$, close to the value obtained for 5CB [43], and $\Delta n_0 = 0.24$.

The present results show an enhanced polarization under an electrical field for the short chain 7OBAF molecule that we ascribed to the presence ferroelectric clusters. An electroconvection phenomenon might also cause a polarization. Patterns typical of electroconvection have not been observed in the present optical microscopy experiments. Because electroconvection is strongly depending on low concentrations of ionic species and alignment conditions, the search of a possible contribution of electroconvection will be the matter of a future work where these parameters will be varied.

3.4. DFT calculations

According to the literature, the stability of the ferroelectric nematic phase is quite sensitive to changes of the polarizability and the dipole moment, which are related to the molecular architecture. To illustrate the impact of these factors, the polarizability tensors, the polarizability anisotropy, the longitudinal and transverse components of the molecular dipole, and dipole moment of 7OBAF have been estimated using DFT calculations at the B3LYP/6-31g(d) level of theory [47]. These parameters are linked to the optical and dielectric properties and are described by the Vuks and the Maier–Meier equations [20,42]:

$$\Delta\varepsilon = \frac{NhF}{\varepsilon_0} \left[\Delta\alpha - \frac{F}{2k_B T} \mu_{\text{eff}}^2 (1-3\cos^2\theta) \right] S \quad (2)$$

where N is the number density of molecules, S is the order parameter, $\Delta\alpha$ is the anisotropy of the polarizability, μ_{eff} is the effective dipole moment of the molecule, θ is the angle between the dipole moment and the long axis of the molecule, F is the feedback factor and h is the cavity factor. The effective dipole moment of the molecule is related to the theoretical value of the dipole moment by the Kirkwood ‘ $g = (\frac{\mu_{\text{eff}}}{\mu})^2$ ’ factor, which describes the degree of parallel/antiparallel correlations between the molecules in the LCs [20,42]. The parallel arrangement is obtained for $g > 1$, while the antiparallel is observed for $g < 1$. The mean polarizability and the polarizability anisotropy of a molecule are defined as follows:

$$\alpha = \frac{\alpha_{xx} + \alpha_{yy} + \alpha_{zz}}{3} \quad (3)$$

$$\Delta\alpha = \alpha_{xx} - \left(\frac{\alpha_{yy} + \alpha_{zz}}{2} \right) \quad (4)$$

The parameters estimated from DFT calculations are summarized in Table 2.

Table 2. Calculated polarizability and dipole moment of 7OBAF molecule.

Parameters	Values
α_x (a.u)	538
α_y (a.u)	528
α_z (a.u)	297
α (a.u)	454.3
$\Delta\alpha$ (a.u)	125.5
μ (Debye)	0.16
N (m ⁻³)	$3 \cdot 10^{26}$
θ (°)	15.5

The low value of the molecular dipole moment of this compound explains the low value of the dielectric anisotropy. This value is much lower than that of 5CB [47]. Furthermore, the number density of molecules N was calculated using the Vuks equations that relate the optical properties to the molecular polarizability and order parameter.

$$\frac{n_0^2-1}{n^2+2} = \frac{N}{3\varepsilon_0} \left(\alpha - \frac{\Delta\alpha S}{3} \right) \quad (5)$$

$$\frac{n_e^2-1}{n^2+2} = \frac{N}{3\varepsilon_0} \left(\alpha + \frac{2\Delta\alpha S}{3} \right) \quad (6)$$

where the parameters of n_e and n_0 are the principal refractive indices along the extraordinary and ordinary ray, respectively. The refractive index (n) is defined by the following equation:

$$n^2 = (n_e^2 + 2n_0^2)/3 \quad (7)$$

The values of n_e , n_0 , $\varepsilon_{//}$ and ε_{\perp} were measured at 105 °C, in the middle of the temperature domain of the nematic phase, and N was deduced. The experimental values of these parameters are presented in Table 3. In addition, h was calculated using the following expression:

$$h = \frac{3\varepsilon}{2\varepsilon+1} \quad (8)$$

It should be mentioned that the empirical method with $F = 1$ in the dipole term of Equation 2 has been used and provided good agreement between calculated and experimental data [46].

Table 3. Experimentally values of optical and dielectric parameters.

Parameters	Values
n_e	1.63
n_0	1.41
n	1.49
$\varepsilon_{//}$	2.83
ε_{\perp}	1.32
ε	3.12
F	1
h	1.3

The high value of the polarizability of this compound may play a great role in the stabilization of the ferroelectric nematic phase. Li et al. [43] have synthesized several polar compounds with high dielectric permittivity and have demonstrated the important contribution of some molecular parameters such as the dipole moment, the geometrical aspect ratio and the angle of dipole moment to the stability of the ferroelectric nematic phase.

The parameters $\Delta\alpha$ and μ_{eff} were estimated from the temperature dependence of $\Delta\epsilon/S$ in the temperature range 100–108 °C. Since these measurements were carried out in a narrow temperature range and not far from the nematic-isotropic transition where the fluctuations are more pronounced, we assumed that $\Delta\alpha$ and μ_{eff} remained constant in the experimental temperature range. In such case, a linear regression was performed on the plot of $\Delta\epsilon/S$ against $1/T$ according to the Maier-Meier model (Equation 2). Figure 11 shows the temperature dependence of $\Delta\epsilon/S$, which showed the expected linear behavior. The effective dipole moment obtained from the slope was 3.6 D, which was much higher than the calculated molecular dipole moment (μ) by DFT. This behavior ($\mu_{\text{eff}} > \mu$) has also been observed in the ferroelectric nematic phase suggesting a parallel distribution [24]; and it was also consistent with the theoretical models [28].

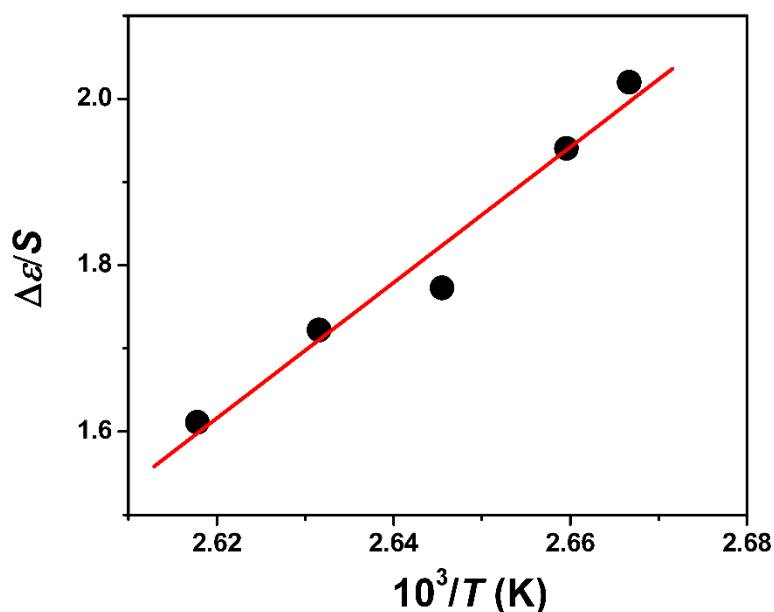


Figure 11. Temperature dependence of $\Delta\epsilon/S$.

The dielectric and electro-optic behaviors are quite different to those obtained in the non-fluorinated homologues nOBA exhibiting the conventional nematic phase [15]. Accordingly, a weak intermolecular interaction by hydrogen bonding involving the fluorine atoms has been considered. Indeed, the high polar nature of C–F bond can produce the polarization of the C–H bonds in the surrounding molecules, leading to the formation of an intermolecular H...F hydrogen bond [48]. Very recently, Merkel et al. have demonstrated that the H...F hydrogen bond played a great role in the stabilization of twist bend nematic liquid crystals [49]. This

behavior indicates that the intermolecular interactions may play a significant role in the stabilization of the ferroelectric nematic phase. In order to get insight into this latter point, several arrangements of interacting molecules were analyzed using DFT calculations. The optimized configuration was obtained when the molecules were positioned parallel with one being shifted with respect to the other along the long molecular axis due to the H...F hydrogen bond (Figure 12). The interaction distance was found to be 2.62 Å, similar but slightly less than that obtained in [43]. In addition, the calculated charge distribution confirmed the existence of the weak intermolecular interaction. Indeed, the hydrogen atoms involved in the H...F hydrogen bond have a larger Millikan charge (0.245 *e*) in this configuration than those in an isolated molecule (0.231 *e*). On the other hand, the fluorine atoms for this configuration have a lower negative Millikan charge (−0.320 *e*) compared to that in an isolated molecule (−0.331 *e*). This result shows a weak intermolecular charge transfer of around 0.014 *e*.

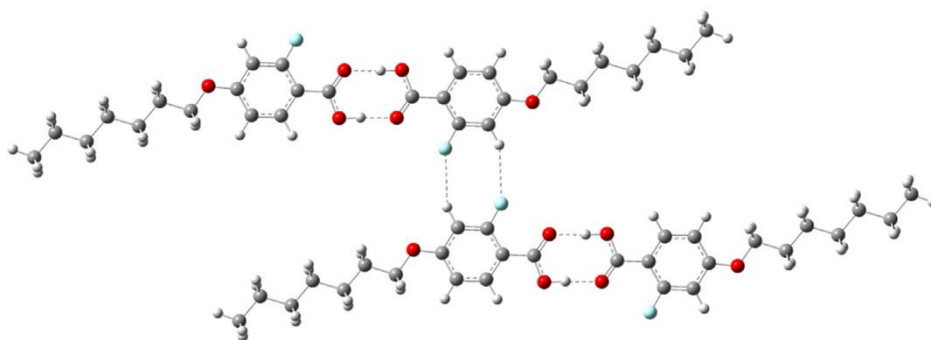


Figure 12. Structure of 7OBAF molecular assemblies obtained by intermolecular hydrogen bonds.

4. Discussion

According to the present work and reports in [24–28,41], the appearance of the ferroelectric clusters in the nematic phase is by far the most common feature in all these instances. This is an effect of the presence of a lateral fluorine substituent and the short alkyl chain. Consequently, not only the dipole moment, but also the polarizability must be considered. Besides, the negative partial charges in the carbon–fluorine bonds present in the molecules could be responsible for the complexation of impurity ions to produce ferroelectric clusters, polar order and therefore spontaneous polarization. Concerning structure-activity relationships, there is an additional force due to the fluorine atoms in 7OBAF that drives a distortion and elastic deformation allowing the appearance of the lower frequency relaxation and electric polarization that was not observed in the non-fluorinated nOBA homologue series. DFT calculations

revealed that the hydrogen bonding intermolecular interaction might play a significant role in the stabilization of the polar nematic phase. This behavior is in agreement with Mandle et al. [42] who showed that the density of the polar nematic phase was significantly higher than in the usual nematic phase. The parallel arrangement driven by the intermolecular interactions in the present compound has a smaller excluded volume than the antiparallel configuration, as observed in other systems [24,26]. Moreover, the increase of the polarization with respect to the decreasing temperature could be explained by the increases of the order parameter and the density upon lowering the temperature according to the following expression:

$$P = \frac{S\mu\rho N_a}{M} \quad (9)$$

where S is the order parameter, μ is the molecular dipole moment, ρ is the density, N_a is the Avogadro number, and M is the molar mass of 70BAF. Using this equation, the calculated polarization value was $1.1 \text{ C}\cdot\mu\text{m}^{-1}$, in good agreement with the experimental value.

5. Conclusions

The supramolecular hydrogen-bonded nematic liquid crystal was synthesized and characterized by elemental analysis and NMR. The formation of H-bonded supramolecular complexes were confirmed by FTIR spectroscopy. The DSC, POM and X-ray diffraction measurements showed that this compound exhibited a nematic phase over a wide temperature range and two crystalline phases. Dielectric measurements disclosed a low frequency relaxation showing the polar behavior of the nematic phase. The induced polarization and dielectric behaviors agreed each other. Both the lower frequency relaxation mode and the value of the polarization are comparable to those obtained in nematic liquid crystals close to their ferroelectric phase. The birefringence, polarizability and the molecular dipole moment calculated by DFT provide a theoretical support to experimental results. In addition, DFT and theoretical calculations of geometrical parameters demonstrated that the lateral fluorine substituent plays a definite role in the appearance of the polar nematic phase with a parallel arrangement of the molecules. This result is in good agreement with theoretical predictions. The higher polarization compared to the nOBAF with longer chain length ($n > 7$) is a remarkable feature of 7OBAF.

Though a ferroelectric phase has not been obtained, these findings may help at exploring new opportunities to design and develop supramolecular assemblies of fluorinated molecules exhibiting stable ferroelectricity behavior and their usefulness in new functional devices.

Acknowledgments: The authors extend their appreciation to funding as the Deanship of Scientific Research at Imam Mohammad Ibn Saud Islamic University. We are grateful to Kai Chung Szeto (CP2M laboratory, University of Lyon 1) for performing C, H elemental analyses.

Funding: The Deanship of Scientific Research at Imam Mohammad Ibn Saud Islamic University, Research Group no. RG-21-09-67.

Conflicts of Interest: The authors declare no conflict of interest.

References

- [1] Asiya S, Pal K, El-Sayyad GS, Abd Elkodous M, Demetriades C, Kralj S, Thomas S. Reliable optoelectronic switchable device implementation by CDS nanowires conjugated bent-core liquid crystal matrix, *Org. Electron.* 2020, 82, 105592, doi:[10.1016/j.orgel.2019.105592](https://doi.org/10.1016/j.orgel.2019.105592).
- [2] Madhu Mohan MLN, Pongali Sathya Prabu N, Pal K. Phase-segregated hydrogen bonded thermotropic liquid crystal's optical shuttering response and electro-optical sensor application. *Mater. Lett.* 2021, 305, 130821, doi:[10.1016/j.matlet.2021.130821](https://doi.org/10.1016/j.matlet.2021.130821).
- [3] Ambrožič M, Pal K, Kralj S, Hölbl A. Nanoparticle controlled nematic macroscopic properties. *J. Mol. Struct.* 2021, 1230, 129878, doi:[10.1016/j.molstruc.2021.129878](https://doi.org/10.1016/j.molstruc.2021.129878).
- [4] Ryzhkova AV, Pratibha R, Nikkhou M, Mušević I. Tuneable ferroelectric liquid crystal microlaser. *Liq. Cryst.* 2020, 47, 994–1003, doi:[10.1080/02678292.2019.1700567](https://doi.org/10.1080/02678292.2019.1700567).
- [5] Ratna BR, Shashidhar R. Dielectric properties of 4'-*n*-alkyl-4-cyanobiphenyls in their nematic phases. *Pramāṇa* 1976, 6, 278–283, doi:[10.1007/BF02872205](https://doi.org/10.1007/BF02872205).
- [6] Lim G, Kikuchi H, Hong S-K. Effect of cyanobiphenyl homologue molecules on electro-optical properties in liquid crystal blue phases and polymer-stabilized blue phases. *Polym. J.* 2014, 46, 337–341, doi:[10.1038/pj.2013.98](https://doi.org/10.1038/pj.2013.98).
- [7] Cui M, Kelly JR. Temperature dependence of visco-elastic properties of 5CB. *Mol. Cryst. Liq. Cryst.* 1999, 331, 49–57, doi:[10.1080/10587259908047499](https://doi.org/10.1080/10587259908047499).
- [8] Wąchała A, Pytlarczyk M, Kula P. On the balance between nematic and smectic phases in 2',3'-difluoro-4,4''-dialkyl-p-terphenyls. *Liq. Cryst.* 2019, 46, 1558–1567, doi:[10.1080/02678292.2019.1590656](https://doi.org/10.1080/02678292.2019.1590656).
- [9] Wang K, Rai P, Fernando A, Szilvási T, Yu H, Abbott NL, Mavrikakis M, Twieg RJ. Synthesis and properties of fluorine tail-terminated cyanobiphenyls and terphenyls for chemoresponsive liquid crystals. *Liq. Cryst.* 2020, 47, 3–16, doi:[10.1080/02678292.2019.1616228](https://doi.org/10.1080/02678292.2019.1616228).

- [10] Saccone M, Kuntze K, Ahmed Z, Siiskonen A, Giese M, Priimagi A. *ortho*-Fluorination of azophenols increases the mesophase stability of photoresponsive hydrogen-bonded liquid crystals. *J. Mater. Chem. C* 2018, 6, 9958–9963, doi:[10.1039/c8tc02611d](https://doi.org/10.1039/c8tc02611d).
- [11] Herman J, Dmochowska E, Pytlarczyk M, Harmata P. Synthesis and mesomorphism of tetrafluoro substituted 4-cyano oligophenyls. *Liq. Cryst.* 2019, 46, 1666–1671, doi:[10.1080/02678292.2019.1593530](https://doi.org/10.1080/02678292.2019.1593530).
- [12] Selvaraj P, Subramani K, Hsu C-J, Huang C-Y. Comparative study on electro-optic effects of organic N-benzyl-2-methyl-4-nitroaniline and morpholinium 2-chloro-4-nitrobenzoate doped in nematic liquid crystals E7. *Polymers* 2020, 12, 2977, doi:[10.3390/polym12122977](https://doi.org/10.3390/polym12122977).
- [13] Spengler M, Dong RY, Michal CA, Pfletscher M, Giese M. Fluorination of supramolecular liquid crystals – tuning tool and analytical probe. *J. Mater. Chem. C* 2017, 5, 2235–2239, doi:[10.1039/c6tc05472b](https://doi.org/10.1039/c6tc05472b).
- [14] Haouas B, Missaoui T, Ben Aissa MA, Jomni F, Arfaoui Y, Soltani T. Synthesis and characterization of lateral fluoro-substituents liquid crystals. *Biointerface Res. Appl. Chem.* 2020, 11, 12495–12505, doi:[10.33263/BRIAC115.1249512505](https://doi.org/10.33263/BRIAC115.1249512505).
- [15] Petrov M, Katranchev B, Rafailov PM, Naradikian H, Dettlaff-Weglikowska U, Keskinova E, Spassov T. Phases and properties of nanocomposites of hydrogen-bonded liquid crystals and carbon nanotubes. *Phys. Rev. E* 2013, 88, 042503, doi:[10.1103/PhysRevE.88.042503](https://doi.org/10.1103/PhysRevE.88.042503).
- [16] Fouzai M, Guesmi A, Ben Hamadi N, Soltani T. Fluoro-substitution in hydrogen bonding liquid crystal benzoic acid: dielectric, electro-optic and optical proprieties and inducing polar nematic phase. *Liq. Cryst.* 2019, 47, 777–784, doi:[10.1080/02678292.2019.1679900](https://doi.org/10.1080/02678292.2019.1679900).
- [17] Arakawa Y, Sasaki Y, Tsuji H. Supramolecular hydrogen- bonded liquid crystals based on 4-*n*-alkylthiobenzoic acids and 4,4'-bipyridine: their mesomorphic behavior with comparative study including alkyl and alkoxy counterparts. *J. Mol. Liq.* 2019, 280, 153–159, doi:[10.1016/j.molliq.2019.01.119](https://doi.org/10.1016/j.molliq.2019.01.119).
- [18] Martínez-Felipe A, Cook AG, Wallage MJ, Imrie CT. Hydrogen bonding and liquid crystallinity of low molar mass and polymeric mesogens containing benzoic acids: a variable temperature Fourier transform infrared spectroscopic study. *Phase Transitions* 2014, 87, 1191–1210, doi:[10.1080/01411594.2014.900556](https://doi.org/10.1080/01411594.2014.900556).
- [19] Nishiya W, Takanishi Y, Yamamoto J, Yoshizawa A. Molecular design for a cybotactic nematic phase. *J. Mater. Chem. C* 2014, 2, 3677–3685, doi:[10.1039/C4TC00001C](https://doi.org/10.1039/C4TC00001C).

- [20] Mandle RJ, Cowling SJ, Goodby JW. A nematic to nematic transformation exhibited by a rod-like liquid crystal. *Phys. Chem. Chem. Phys.* 2017, 19, 11429–11435, doi:[10.1039/c7cp00456g](https://doi.org/10.1039/c7cp00456g).
- [21] Mandle RJ, Cowling SJ, Goodby JW. Rational design of rod-like liquid crystals exhibiting two nematic phases. *Chem. Eur. J.* 2017, 23, 14554–14562, doi:[10.1002/chem.201702742](https://doi.org/10.1002/chem.201702742).
- [22] Nishikawa H, Shiroshita K, Higuchi H, Okumura Y, Haseba Y, Yamamoto S-i, Sago K, Kikuchi H. A fluid liquid-crystal material with highly polar order. *Adv. Mater.* 2017, 29, 1702354, doi:[10.1002/adma.201702354](https://doi.org/10.1002/adma.201702354).
- [23] Missaoui T, Ben Amor I, Soltani T, Ben Ouada H, Jeanneau E, Chevalier Y. Dielectric and electro-optic properties of cybotactic nematic phase in hydrogen-bonded liquid crystals. *J. Mol. Liq.* 2020, 304, 112726–112734, doi:[10.1016/j.molliq.2020.112726](https://doi.org/10.1016/j.molliq.2020.112726).
- [24] Chen X, Dong D, Clark NA. First-principles experimental demonstration of ferroelectricity in a thermotropic nematic liquid crystal: Polar domains and striking electro-optics. *Proc. Natl. Acad. Sci. USA* 2020, 117, 14021–14031, doi:[10.1073/pnas.2002290117](https://doi.org/10.1073/pnas.2002290117).
- [25] Manabe A, Bremer M, Kraska M. Ferroelectric nematic phase at and below room temperature. *Liq. Cryst.* 2021, 48, 1079–1086, doi:[10.1080/02678292.2021.1921867](https://doi.org/10.1080/02678292.2021.1921867).
- [26] Sebastián N, Cmok L, Mandle RJ, de la Fuente MR, Drevenšek Olenik I, Čopič M, Mertelj A. Ferroelectric-ferroelastic phase transition in a nematic liquid crystal. *Phys. Rev. Lett.* 2020, 124, 037801, doi:[10.1103/PhysRevLett.124.037801](https://doi.org/10.1103/PhysRevLett.124.037801).
- [27] Saha R, Nepal P, Feng C, Hossain MS, Fukuto M, Li R, Gleeson JT, Sprunt S, Twieg RJ, Jákli A. Multiple ferroelectric nematic phases of a highly polar liquid crystal compound. *Liq. Cryst.* 2022, 49, 1784–1796, doi:[10.1080/02678292.2022.2069297](https://doi.org/10.1080/02678292.2022.2069297).
- [28] Born M. Über anisotrope Flüssigkeiten. Versucheiner Theorie der flüssigen Kristalle und des elektrischen Kerr-Effekts in Flüssigkeiten. *Sitzungsber. Preuss. Akad. Wiss.* 1916, 30, 614–650.
- [29] Éber N, Salamon P, Buka Á. Electrically induced patterns in nematics and how to avoid them. *Liq. Cryst. Rev.* 2016, 4, 101–134, doi:[10.1080/21680396.2016.1244020](https://doi.org/10.1080/21680396.2016.1244020).
- [30] Xu ZD, He YN, Guo MC, Wang XG. Alternating current electric-field-induced tunable microstructures and electrohydrodynamic convection properties observed in azo-dye-doped MBBA liquid crystal cells. *J. Appl. Phys.* 2007, 102, 026101, doi:[10.1063/1.2753577](https://doi.org/10.1063/1.2753577).
- [31] Zhang Y, Yang X, Zhan Y, Zhang Y, He J, Lv P, Yuan D, Hu X, Liu D, Broer DJ, Zhou G, Zhao W. Electroconvection in zwitterion-doped nematic liquid crystals and application as smart windows. *Adv. Optical Mater.* 2020, 9, 2001465, doi:[10.1002/adom.202001465](https://doi.org/10.1002/adom.202001465).

- [32] Urbanski M, Kinkead B, Qi H, Hegmann T, Kitzerow H-S. Electroconvection in nematic liquid crystals *via* nanoparticle doping. *Nanoscale* 2010, 2, 1118–1121, doi:[10.1039/c0nr00139b](https://doi.org/10.1039/c0nr00139b).
- [33] Dolgov L, Yaroshchuk O, Lebovka M. Effect of electro-optical memory in liquid crystals doped with carbon nanotubes. *Mol. Cryst. Liq. Cryst.* 2008, 496, 212–229, doi:[10.1080/15421400802451816](https://doi.org/10.1080/15421400802451816).
- [34] Lee K-W, Posche T. Electroconvection of pure nematic liquid crystals without free charge carriers. *Soft Matter* 2017, 13, 8816–8823, doi:[10.1039/c7sm02055d](https://doi.org/10.1039/c7sm02055d).
- [35] Kramer L, Pesch W. Convection instabilities in nematic liquid crystals. *Annu. Rev. Fluid Mech.* 1995, 27, 515–541, doi:[10.1146/annurev.fl.27.010195.002503](https://doi.org/10.1146/annurev.fl.27.010195.002503).
- [36] Madhu Mohan MLN, Pal K. Camphoric acid based ferroelectric hydrogen bonded liquid crystalline materials integration further dielectric relaxations and novel applications. *J. Mol. Struct.* 2021, 1232, 130022, doi:[10.1016/j.molstruc.2021.130022](https://doi.org/10.1016/j.molstruc.2021.130022).
- [37] Soltani T, Bitri N, Dhaouadi H, Gharbi A, Marcerou JP, Nguyen HT. Synthesis, characterisation and behaviour under a field of a chiral smectic liquid crystal. *Liq. Cryst.* 2009, 36, 1329–1336, doi:[10.1080/02678290903220998](https://doi.org/10.1080/02678290903220998).
- [38] Soltani T, Chemingui M, Bouaziz N, Marcerou JP, Othman T. Electric field induced transformations and dielectric properties of ferrielectric smectic phase. *J. Mol. Liq.* 2014, 199, 162–166, doi:[10.1016/j.molliq.2014.09.007](https://doi.org/10.1016/j.molliq.2014.09.007).
- [39] Bibonne F, Parneix JP, Nguyen HT. Relaxation processes in the ferrielectric and alpha phases of antiferroelectric liquid crystals. *Eur. Phys. J. AP* 1998, 3, 237–241, doi:[10.1051/epjap:1998226](https://doi.org/10.1051/epjap:1998226).
- [40] Li J, Wang Z, Deng M, Zhu Y, Zhang X, Xia R, Song Y, Hisai Y, Aya S, Huang M. General phase-structure relationship in polar rod-shaped liquid crystals: Importance of shape anisotropy and dipolar strength. *Giant* 2022, 11, 10010, doi:[10.1016/j.giant.2022.100109](https://doi.org/10.1016/j.giant.2022.100109).
- [41] Mandle RJ, Sebastián N, Martínez-Perdiguero J, Mertelj A. On the molecular origins of the ferroelectric splay nematic phase. *Nat. Commun.* 2021, 12, 4962, doi:[10.1038/s41467-021-25231-0](https://doi.org/10.1038/s41467-021-25231-0).
- [42] Ju S-P, Huang S-C, Lin K-H, Chen H-Y, Shen T-K. Prediction of optical and dielectric properties of 4-cyano-4-pentylbiphenyl liquid crystals by molecular dynamics simulation, coarse-grained dynamics simulation, and density functional theory calculation. *J. Phys. Chem. C* 2016, 120, 14277–14288, doi:[10.1021/acs.jpcc.5b12222](https://doi.org/10.1021/acs.jpcc.5b12222).

- [43] Li J, Nishikawa H, Kougo J, Zhou J, Dai S, Tang W, Zhao X, Hisai Y, Huang M, Aya S. Development of ferroelectric nematic fluids with giant- ϵ dielectricity and nonlinear optical properties. *Sci. Adv.* 2021, 7, 5047, doi:[10.1126/sciadv.abf5047](https://doi.org/10.1126/sciadv.abf5047).
- [44] Yang D, Wu S. *Fundamentals of Liquid Crystal Devices*. John Wiley & Sons: Hoboken, NJ, USA, 2006.
- [45] Basumatary J, Nath A, Devi TK. Temperature effects on optical parameters of liquid crystal binary mixtures exhibiting induced smectics phases. *J. Mol. Liq.* 2020, 311, 113251, doi:[10.1016/j.molliq.2020.113251](https://doi.org/10.1016/j.molliq.2020.113251).
- [46] Xu M-Y, Zhou M-j, Xiang Y, Salamon P, Éber N, Buka Á. Domain structures as optical gratings controlled by electric field in a bent-core nematic. *Opt. Express* 2015, 23, 15224–15234, doi:[10.1364/OE.23.015224](https://doi.org/10.1364/OE.23.015224)
- [47] Frisch MJ, Trucks GW, Schlegel HB, et al. *Gaussian 09, Revision A.02*; Gaussian Inc.: Wallingford, CT, USA, 2009, 200.
- [48] Hird M. Fluorinated liquid crystals – properties and applications. *Chem. Soc. Rev.* 2007, 36, 2070–2095, doi:[10.1039/b610738a](https://doi.org/10.1039/b610738a).
- [49] Merkel K, Loska B, Welch Ch, Mehl GH, Kocot A. The role of intermolecular interactions in stabilizing the structure of the nematic twist-bend phase. *RSC Adv.* 2021, 11, 2917–2925, doi:[10.1039/D0RA10481G](https://doi.org/10.1039/D0RA10481G).

SUPPLEMENTARY INFORMATION

Polar Nematic Phase in Short-Chained Fluorinated Hydrogen-Bonded Liquid Crystals

Malek Fouzai¹, Philippe Dieudonné-George², Ahlem Guesmi³, Naoufel Ben Hamadi³, Youssef Arfaoui⁴, Taoufik Soltani^{1,*}, Yves Chevalier⁵

¹ Université de Tunis El Manar, Faculté des Sciences de Tunis, Laboratoire de Physique de la Matière Molle et de la Modélisation Électromagnétique (LR99ES16), 2092 Tunis, Tunisia.

² Laboratoire Charles Coulomb, UMR 5221, CNRS-Université de Montpellier, 34095 Montpellier, France.

³ Chemistry Department, College of Science, Imam Mohammad Ibn Saud Islamic University (IMSIU), Riyadh, Kingdom of Saudi Arabia.

⁴ Université de Tunis El Manar, Faculté des Sciences de Tunis, Laboratoire de Caractérisations, Applications et Modélisation de Matériaux (LR18ES08), 2092 Tunis, Tunisia.

⁵ Université Claude Bernard Lyon 1, Laboratoire d'Automatique, de Génie des Procédés et de Génie Pharmaceutique (LAGEPP), CNRS UMR 5007, 43 bd 11 Novembre, 69622 Villeurbanne Cedex, France.

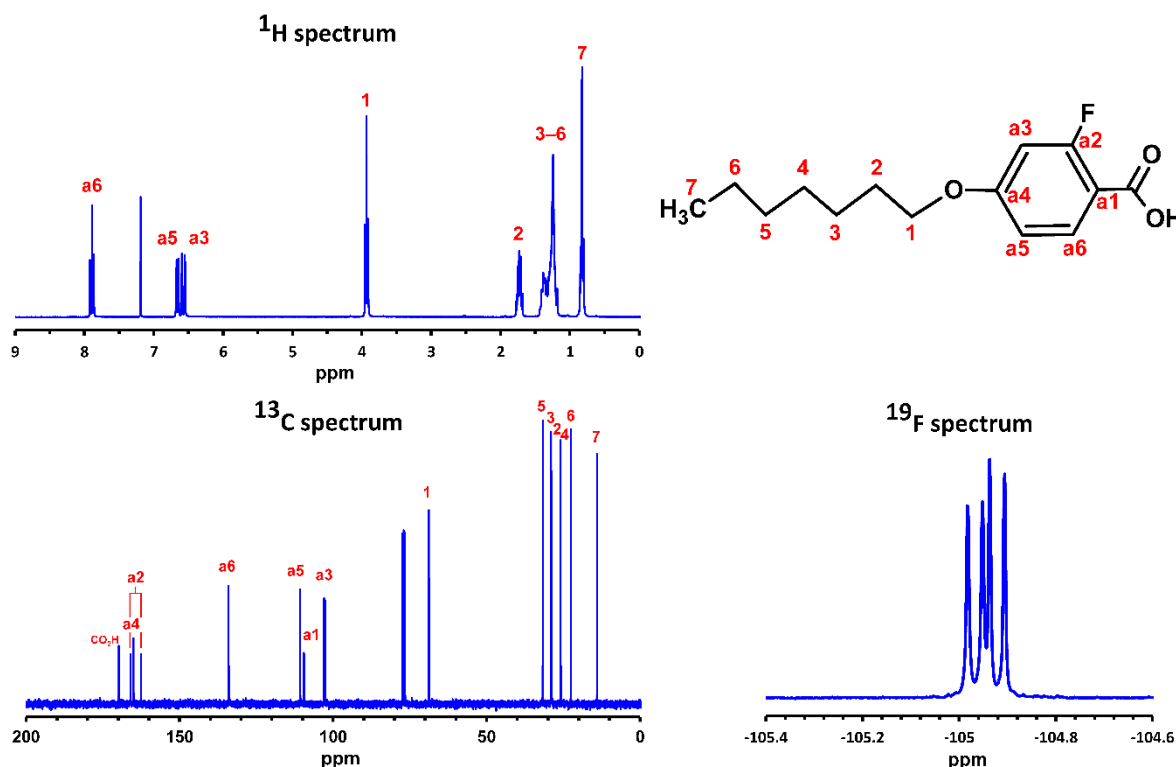


Figure S1. ^1H , ^{13}C and ^{19}F NMR spectra of 7OBAF in CDCl_3 solution.

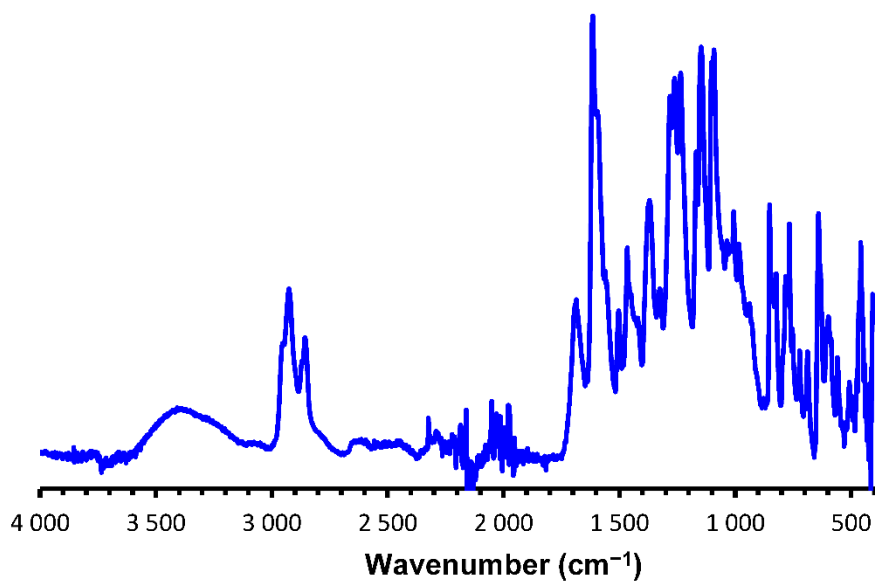


Figure S2. IR spectrum of 7OBAF.

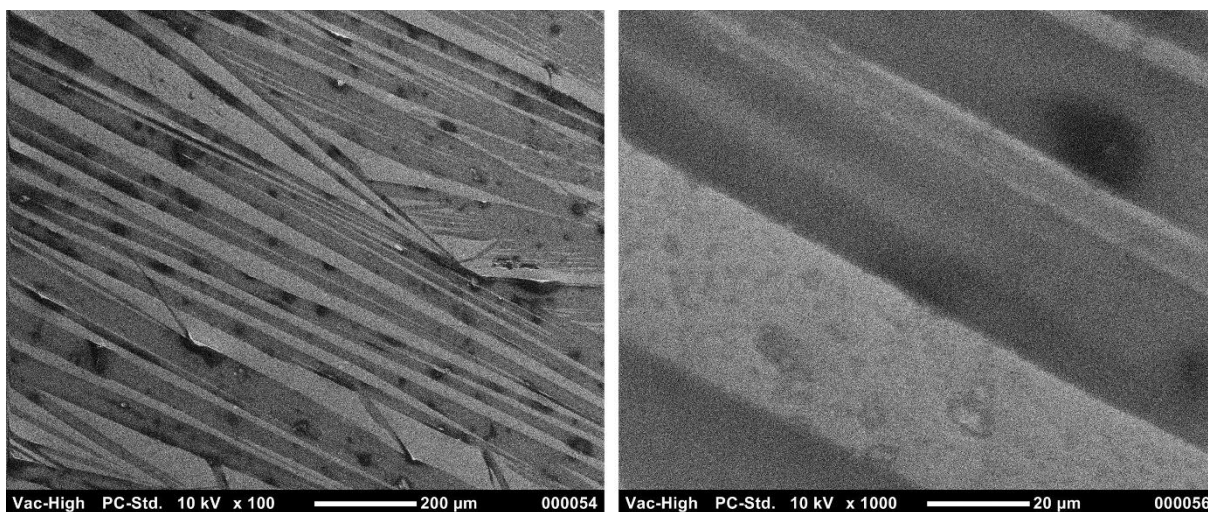


Figure S3. SEM pictures at different magnifications of a thin film of 7OBAF cast on the ITO surface of a glass plate.

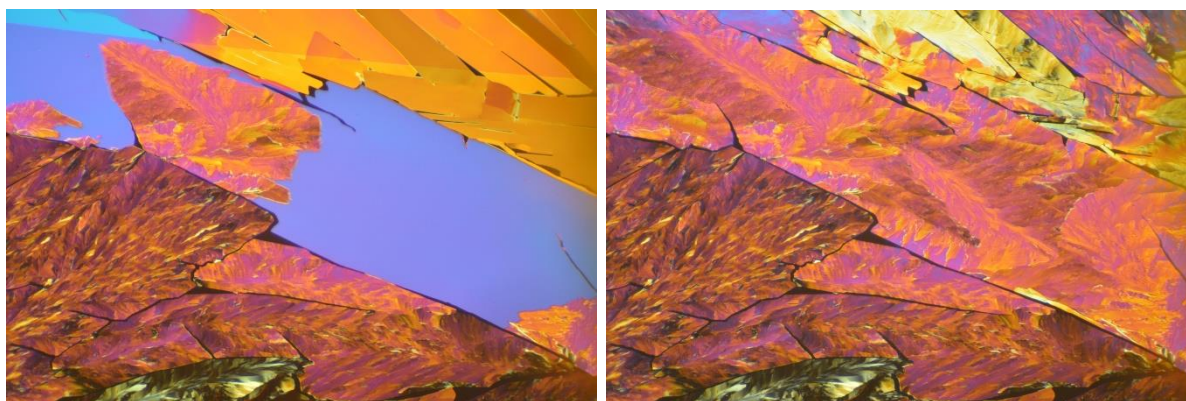


Figure S4. (Left) 7OBAF Cr2→Cr1 phase transition observed in POM when cooling a single crystals at 50 °C. (Right) Resulting texture after the phase transition.

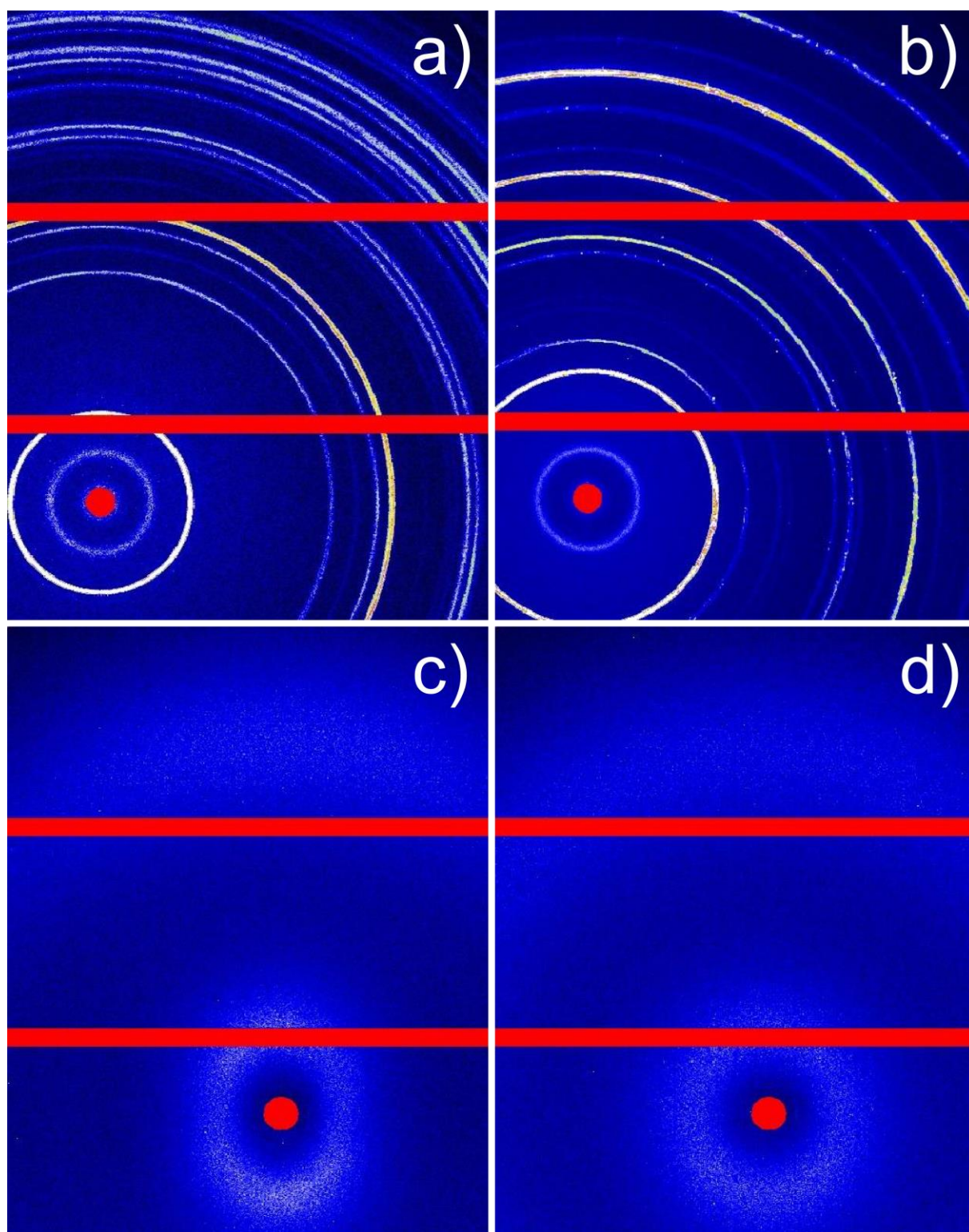


Figure S5. 2D powder WAXS patterns of 7OBAF for the different phases obtained at increasing temperatures: a) Cr1 (75 °C), b) Cr2 (80 °C), c) N (105 °C) d) I (115 °C). The diffractograms shown in the main text correspond to the angular average of these patterns.